CrossMark

Effects of α-Al$_2$O$_3$ nanoparticles-doped on microstructure and properties of Sn–0.3Ag–0.7Cu low-Ag solder

Jie Wu[1] · Songbai Xue[1] · Jingwen Wang[1] · Mingfang Wu[2] · Jianhao Wang[1]

Abstract

In order to enhance the properties of Sn–0.3Ag–0.7Cu low-Ag solder, α-Al$_2$O$_3$ nanoparticles with various content (0–0.5 wt%) were successfully doped into the solder paste with a self-designed dispersion step. After comprehensive study of the microstructures and properties of the novel nano-composite solder, several satisfactory modified results can be obtained. For instance, the wettability of solder was greatly improved with trace amount of α-Al$_2$O$_3$ nanoparticles-doped. The superior wettability was achieved by Sn–0.3Ag–0.7Cu–0.12Al$_2$O$_3$ solder with spreading area approaching to ~ 79 mm^2. Detailed thermodynamic and kinetic analysis of how α-Al$_2$O$_3$ nanoparticles promoting the processes of solder wetting and spreading on Cu substrate were given. In addition, the joint soldered with Sn–0.3Ag–0.7Cu–0.12Al$_2$O$_3$ displayed the highest shear force (57.1 N) with a typical ductile fracture failure mode. This relates to the evidently refined microstructure as well as the well-controlled growth of interfacial Cu$_6$Sn$_5$ IMCs. Corresponding theoretical analysis shows 0.12 wt% Al$_2$O$_3$ nanoparticles-doped can decrease the growth rate constant of interfacial Cu$_6$Sn$_5$ IMCs from 5.08×10^{-10} to 1.71×10^{-10} cm^2/s.

1 Introduction

In the past few years, traditional Sn–Pb solders have been extensively banned in electronic packaging by the international legislations (WEEE and RoHS directives) owing to the toxic effects of lead in Sn–Pb solders [1]. So, investigations on lead-free solders to replace Sn–Pb solders became extremely essential. So far the alternatives having been put into use mainly includes binary systems of Sn–Ag, Sn–Cu, Sn–Zn and ternary systems of Sn–Ag–Cu, Sn–Cu–Ni, Sn–Zn–Bi [2, 3]. Among them, Sn–Ag–Cu near-eutectic high-Ag solders (Ag content: 3.0–3.9 wt%) were attached particular importance due to their superior comprehensive performance (e.g., wettability, thermal–mechanical reliabilities). Unfortunately, besides relative high production cost caused by high price of valuable metal Ag, Sn–Ag–Cu high-Ag solders still faced some performance issues, such

as low drop impact reliability due to the appearance of large Ag$_3$Sn IMCs [4, 5]. So, lowering Ag content in Sn–Ag–Cu solders became essential. Even so, Sn–Ag–Cu low-Ag solders still encountered some new issues on basic properties, such as relatively higher melting point, poor wettability and the degraded mechanical strengths [6–8].

In order to compensate for these deficiencies and further modify relevant properties of Sn–Ag–Cu low-Ag solders, various foreign alloys (e.g., Bi [9], Ni [10], Zn [11], rare eath (RE) [12, 13]) were selected to be doped. It was found low-Ag solders doped with RE elements displayed better performances than other alloys due to their distributions at grain boundaries playing a role of pinning boundaries' motions. However, their doped contents are worthwhile to be noted [14]. For instance, Ga with excessive content in Sn–Ag–Cu solder produced bulk Cu–Ga phases with degradation potential to the mechanical strengths of solder joint [15]. In addition, large amount of hard and brittle Sn–RE phases emerged in excessive RE-doped solder, which were the birthplaces of Sn whiskers, conductive metal wires that may induce short circuits and finally break the normal work condition of electronic devices [12]. So, researchers began to switch their attentions to other additives, such as nanoparticles or nanosheets, popular in various fields in recent years [16–18]. This is because nano-scale particles or sheets present many specific features, such as

✉ Songbai Xue
xuesb@nuaa.edu.cn

[1] College of Materials Science and Technology, Nanjing University of Aeronautics and Astronautics, Nanjing 210016, People's Republic of China

[2] School of Materials Science and Engineering, Jiangsu University of Science and Technology, Zhenjiang 212003, People's Republic of China

extremely high surface energy, large specific surface area, better electrical conductivity and so on [19]. A few satisfactory properties were obtained by solders doped with various kinds of nanoparticles or nanosheets, such as nano-metal nanoparticles (e.g., nano-Ni [20], nano-Al [21]), nano-carbides (e.g., graphite nanosheets (GNSs) [22], single-walled carbon nanotubes (SWCNTs) [23], Ni-coated nanosheets (Ni-CNTs) [24]) and nano-ceramic particles (e.g., ZrO_2 [25], ZnO [26]). The joint soldered with Ni nanoparticles-doped Sn–3.8Ag–0.7Cu solder presented a well-controlled planar-like (Cu, Ni)–Sn interfacial IMC layer, a potential microstructure reason to get a reliable bonding [20]. In addition, Sn–3.8Ag–0.7Cu–0.05SWCNTs were reported to be successfully fabricated by means of homogeneously mixing Sn–3.8Ag–0.7Cu particles with SWCNTs through a V-cone blender. This newly developed nanoparticles-doped solder was found to display both obviously increased yield and ultimate tensile strengths without affecting total elongation at all studied temperatures (25–75 °C) and strain rates (5×10^{-4} to 5×10^{-2} s^{-1}) [22]. In order to get a firm combination between solder matrix and foreign carbon nanotubes, Ni-coated carbon nanotubes were made and doped into the Sn–3.5Ag–0.7Cu solders [24]. As expected, this composite solder joint displayed much higher tensile strength and creep resistance than its counterpart. Moreover, solders doped with non-reacting and non-coarsening ceramic nanoparticles (e.g., ZrO_2 [25], ZnO [26]) also presented a series of particularly improved properties, especially in the mechanical properties and creep resistance. It can be concluded that there have been many researches on the effects of nanoparticles-doped on properties of Sn–Ag–Cu high-Ag solders, but few on those of Sn–Ag–Cu low-Ag solders. This is because the technique of doping nanoparticles into solder was still immature with some unresolved issues like agglomerations, which can't be resolved thoroughly only by mechanical stirring [19]. So far, investigations on low-Ag solders modified by nanoparticles also claimed these foreign nanoparticles played the positive effects on modifying properties of solders and mechanical stirring is still a main method to avoid agglomerations. Zhang et al. [27] once manually mixed Al nanoparticles into Sn–1Ag–0.5Cu solder paste and found that Al nanoparticles reinforced solder performed overall better properties (e.g., wettability, mechanical properties) than its counterpart. In addition, Yang et al. [28] blended Sn–1.0Ag–0.5Cu particles (45 μm) with $BaTiO_3$ nanoparticles using a roller blender (speed speed: 200 rmp/h) to fabricate $BaTiO_3$ nanoparticles-doped Sn–1.0Ag–0.5Cu solder. It was found this newly composite solder displayed a relatively high UTS value of 53.85 MPa, about 19% higher than the non-modfied solder. In addition, Fe_2O_3 nanoparticles-doped Sn–1.0Ag–0.7Cu solder made by smelting method had a much better wettability than the non-doped solder. Also, the growth of interfacial Cu_6Sn_5 IMCs at the modified solder/Cu

interface was remarkably inhibited [29]. By comparison, it can be obtained that non-coarsening refractory nanoparticles exert higher impact on enhancing mechanical properties or improving creep resistance of solders than other kinds of nanoparticles since non-coarsening refractory nanoparticles can serve as numerous extra stable obstacles to impede dislocations' motions.

Alumina (Al_2O_3) nanoparticles, one kind of ceramics, are widely applied as reinforcements due to their superiorities in heat stability, availability as well as low cost. It was found that Al_2O_3 nanoparticles-doped eutectic Sn–9Zn solder (diameter: ~ 50 nm) made by means of melting solders with Al_2O_3 nanoparticles wrapped in Zn foil displayed better wettability and evidently increased shear force [30]. Tsao et al. [31] once mixed Al_2O_3 nanoparticles (diameter: ~ 100 nm) into Sn–3.5Ag–0.7Cu solder paste and found that the corresponding solder joint had an distinctly suppressed Cu_6Sn_5 IMC layer and thus performing an improved shear strength. However, its wettability was not studied. It should be noted that nearly no prior reports investigated on the effects of Al_2O_3 nanoparticles on properties of low-Ag solders, let alone on those of super low-Ag (0.3 wt%) solders. Most importantly, in the former investigations, we can't ensure a full dispersion of nanoscale Al_2O_3 particles in solder just with a simple mechanical mixing and without any previous dispersed treatment.

So, in order to study the effects of refractory Al_2O_3 nanoparticles-doped on relevant properties (e.g., wetability, shear force and creep resistance) of Sn–0.3Ag–0.7Cu super low-Ag solder, Al_2O_3 nanoparticles were mechanically mixed into the super low-Ag solder paste with a previous self-designed dispersion step to avoid agglomerations of Al_2O_3 nanoparticles. In addition, detailed mechanisms of how Al_2O_3 nanoparticles with suitable amount promoting processes of solder wetting and spreading on Cu substrate were also given. Moreover, the evolutions of their microstructures after doping Al_2O_3 nanoparticles were also studied to better understand their properties' changes.

2 Experimental

2.1 Material preparation

Sn–0.3Ag–0.7Cu low-Ag solder paste with average powder diameter of 20–38 μm was bought from JPT solder Co. Ltd. in ShenZhen, China. Also, Al_2O_3 nanoparticles were commercially available with average size around 50 nm, whose morphology was given in Fig. 1a. Figure 1b provided X-ray diffraction (XRD, 40 kV (100 mA), scanning speed: 4°/min) analyzed result of Al_2O_3 nanoparticles to realize phase detection. After compared with the standard atlas, these nanoparticles were ascertained as α-Al_2O_3 nanoparticles.
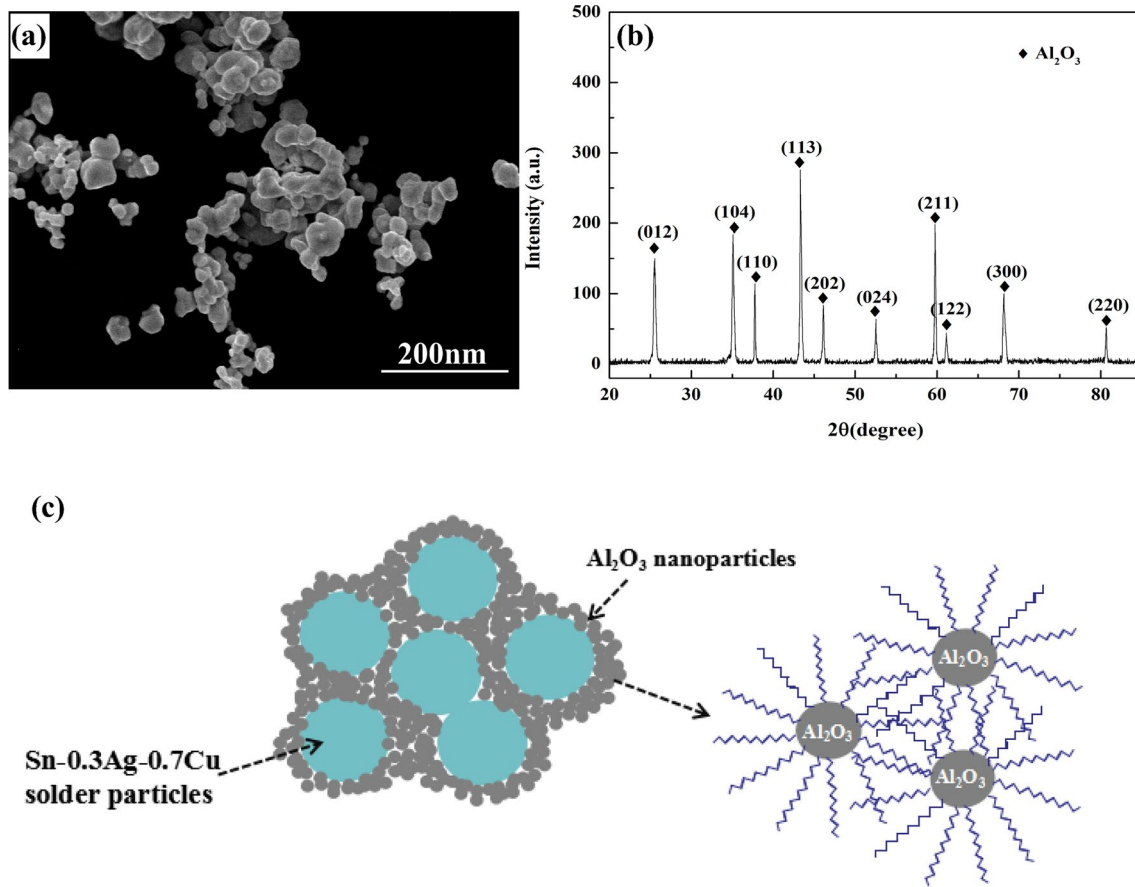
Fig. 1 **a** FE-SEM micrograph of Al_2O_3 nanoparticles; **b** XRD spectrum of Al_2O_3 nanoparticles; **c** schematic diagram of Al_2O_3 nanoparticles-doped Sn–0.3Ag–0.7Cu solder paste

In order to avoid their agglomerations, α-Al_2O_3 nanoparticles with different nominal content (0–0.5 wt%) were firstly dispersed in absolute alcohol with ultrasonic vibration for 30 min. Then, appropriate percent (~0.5 wt%) of polyethylene glycol (PEG-2000, analytical grade) as dispersant was added into the above-vibrated α-Al_2O_3 nanoparticles alcohol solution to further disperse α-Al_2O_3 nanoparticles [32]. This is because that one end of molecular chain of PEG-2000 is easy to establish a strong hydrogen bond with the surface of α-Al_2O_3 nanoparticles, while the molecular chain into ethanol solution expands and form an adsorption layer with a certain thickness, as shown in Fig. 1c. When nanoparticles are close to each other, the steric hindrance effect of this thick polymer film greatly weakens the attraction between nanoparticles [33]. So, the agglomerations were greatly suppressed. Afterwards, procedures of centrifugation and drying were conducted to clean away the alcohol and PEG-2000. Finally, α-Al_2O_3 nanoparticles with different amount were mechanically mixed into Sn–0.3Ag–0.7Cu solder paste with glass rod uniformly stirring for 30 min. It should be noted here that extremely minute quantity of PEG residue

is inconsequential since the remaining PEG in solder paste can serve as the partial film forming agent during the reflow process [34].

2.2 Melting point and wettability

Melting points of Sn–0.3Ag–0.7Cu–xAl_2O_3 solders were measured by differential scanning calorimetry (DSC; Netzsch DSC 200F3). The weight of each tested nano-Al_2O_3 containing solders is 10 mg. The heating temperature range is from 25 to 280 °C. The scanning rate is 5 °C/min. In addition, the whole process was shielded by pure nitrogen flow.

The wettability of α-Al_2O_3 nanoparticles-doped Sn–0.3Ag–0.7Cu solders were evaluated by spreading area according to Chinese National Standard GB11364-2008. Before test, each content of α-Al_2O_3 nanoparticles-doped solder paste (0.2 ± 0.01 g) was placed on a copper substrate (40 mm × 40 mm × 0.2 mm) cleaned with acetone and alcohol. Then, samples were put in a resistance furnace with temperature change following the reflow profile in Fig. 2a.
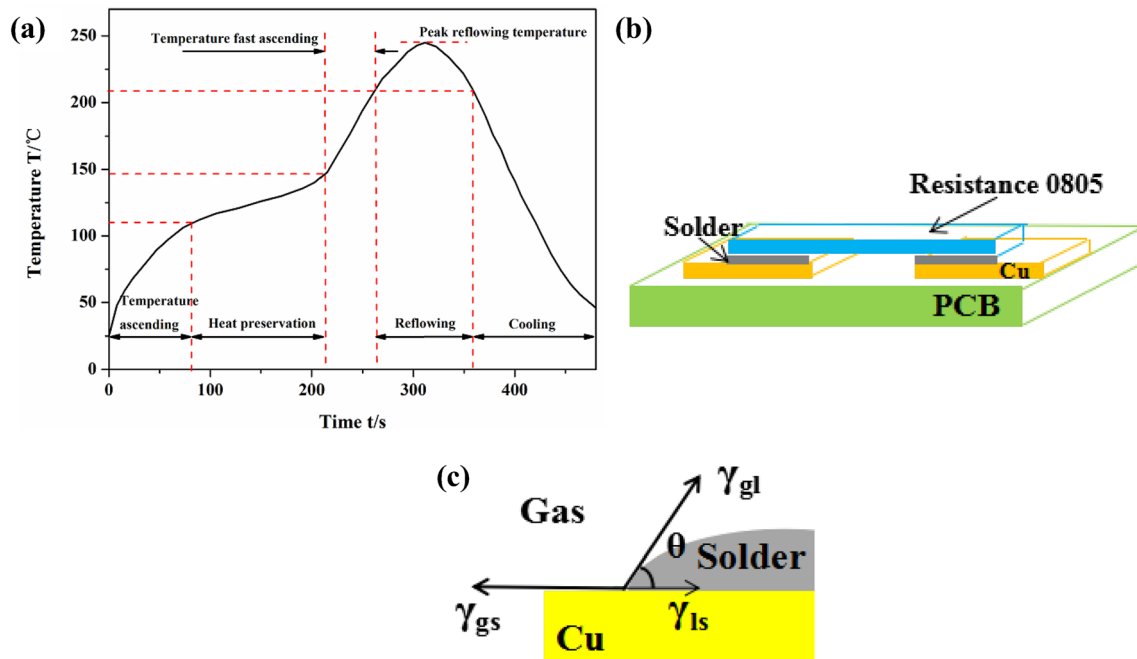
Fig. 2 **a** Reflowing profile for Al_2O_3 nanoparticles-doped Sn–0.3Ag–0.7Cu solders; **b** schematic diagram of soldering sample; **c** schematic diagram of solder spreading on Cu substrate in equilibrium

Thus, spreading samples can be obtained and Image-J software was applied to conduct spreading area measurement.

2.3 XRD analysis and microstructure observation

Before microstructure observation, all the samples were firstly ground with sandpaper, polished with 2.5 µm diamond paste and etched with 4% HNO_3-alcohol then. Finally, microstructure observation and phases analysis were realized with the aid of optical microscope (OM), scanning electron microscope (SEM) equiped with energy dispersive X-ray spectrum (EDS). In addition, as for interfacial microstructure observation, representative Sn–0.3Ag–0.7Cu–xAl_2O_3/Cu (x = 0, 0.12 and 0.5 wt%) samples were selected. Likewise, after basic grind and polish treatment, the backscattered electron (BSE) image mode in SEM was selected to observe the evolutions of interfacial IMC layers at the solders/Cu interfaces, whose thickness can be calculated also with the Image-J software based on the following equation:

$$\bar{t} = \frac{A_i}{l_i}, \tag{1}$$

where $\bar{t}$ is the average thickness of interfacial IMC layer; A_i represents the total calculated area; l_i stands for the length of the measured IMC layer.

2.4 Mechanical properties

Before shear force test, chip resistors (0805, $2 \times 1.2 \times 0.5$ mm^3) were placed on the corresponding Cu foils attached on printed circuit board (PCB) with α-Al_2O_3 nanoparticles-doped solder pastes serving as solders (Fig. 2b). Afterwards, samples were put in a reflow oven with temperature change following the designed reflow curve in Fig. 2a. Finally, STR-1000 Micro-joint strength tester (Rhesca Co., Ltd, Japan) was used to measure the shear force of these samples. In order to further understand the effect of nano-Al_2O_3 particles on shear force, typical shear fracture surfaces were also selected to be observed and analyzed by SEM/EDS technique.

3 Results and discussion

3.1 Melting characteristic

Figure 3 depicts the DSC curves of Sn–0.3Ag–0.7Cu–xAl_2O_3 solders (x = 0–0.5 wt%) during heating and cooling process. Clearly, the endothermic peaks on the heating process (Fig. 3a) correspond to the melting points of solders, as summarized in Table 1. As can be seen, the melting points of solder alloys are slightly decreased after doping trace amount of α-Al_2O_3 nanoparticles. This implies no
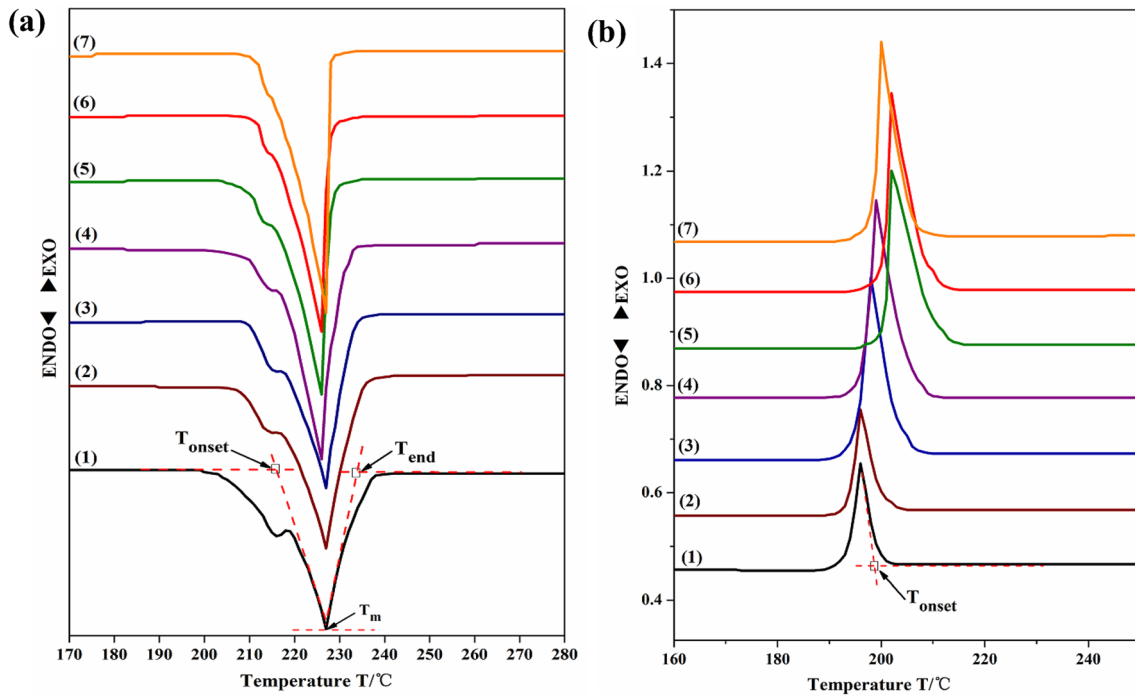
Fig. 3 DSC curves of **a** heating (endothermal) and **b** cooling (exothermal) process of Sn–0.3Ag–0.7Cu–xAl$_2$O$_3$ solders [x=(_1_) 0; (_2_) 0.015 wt%; (_3_) 0.03 wt%; (_4_) 0.06 wt%; (_5_) 0.12 wt%; (_6_) 0.5 wt%; (_7_) 0.5 wt%]

Table 1 Melting parameters of Sn–0.3Ag–0.7Cu–xAl$_2$O$_3$ solder (x = 0–0.5 wt%)

Solder alloy	Melting parameters					
	Parameters during heating				Parameters during cooling	
	T_{onset} (T_{Ho})/°C	T_{end}/°C	Pasty range ($T_{end} - T_{onset}$)/°C	Peak temperature/°C	T_{onset} (T_{Co})/°C	Undercooling ($\Delta T = T_{Ho} - T_{Co}$)/°C
(a) SAC0307	217.1	234	16.9	227	198.7	18.4
(b) SAC0307-0.015Al$_2$O$_3$	216.8	232.5	15.7	227	200.3	16.5
(c) SAC0307-0.03Al$_2$O$_3$	216.4	230.8	14.4	226.5	203	13.4
(d) SAC0307-0.06Al$_2$O$_3$	216.3	229.1	12.8	226.2	206.5	9.8
(e) SAC0307-0.12Al$_2$O$_3$	216.1	227	10.9	226	210.2	5.9
(f) SAC0307-0.25Al$_2$O$_3$	216.1	227.4	11.3	226.3	208.9	7.2
(g) SAC0307-0.5Al$_2$O$_3$	216.2	227.6	11.4	226.5	206.1	10.1

SAC0307 represents Sn–0.3Ag–0.7Cu

requirements to adjust the original soldering parameters when using this α-Al$_2$O$_3$ nanoparticles-doped solder. Ref. [30] also reported the similar changes of the melting points of Sn–Zn solder after doping Al$_2$O$_3$ nanoparticles. Table 1 also presents the pasty range ($T_{end} - T_{onset}$ on the heating process) of Sn–0.3Ag–0.7Cu–xAl$_2$O$_3$ solders, an evaluation of wettability due to its determination in the time of solder in liquid state during soldering process. Remarkably, with increasing the content of nano-Al$_2$O$_3$ particles, the pasty range of solder has a decrease first but with a trifling increase later. So, the minimum value (10.9 °C) exists at the

point of 0.12 wt%, indicating Sn–0.3Ag–0.7Cu–0.12Al$_2$O$_3$ solder has a complete melting with much more rapid rate than the original one during soldering process, as reflected in the changes in wettability. Moreover, undercooling, a significant index to evaluate the solidification rate of molten solder, is defined as the difference between T_{onset} upon heating and T_{onset} upon cooling (Fig. 3b) in the DSC curves. Relative data has been summarized in Table 1, from which, we can see that the solder doped 0.12 wt% α-Al$_2$O$_3$ nanoparticles had the lowest undercooling (5.9 °C), about 67.9% smaller than the original. This is because α-Al$_2$O$_3$ nanoparticles can

serve as extra nucleation sites to accelerate solidification process, especially that of β-Sn phases.

3.2 Wettability

Wettability of solder, a significantly crucial property that determines the mechanical properties and reliability of solder joint. In this study, the wettability were evaluated by spreading area (*S*) and the larger the "S" is, the better the wettability. Figure 4a shows the spreading macroscopic morphologies of Sn–0.3Ag–0.7Cu–0.12Al$_2$O$_3$ solders. As can be directly seen, with increasing α-Al$_2$O$_3$ nanoparticles, the spreading area of solder increases first but with a later decline as α-Al$_2$O$_3$ nanoparticles continue to be doped. It can be seen From Fig. 4b, the bar graph of measured spreading areas as the function of the nanoparticles' content, the maximum value of spreading area of Sn–0.3Ag–0.7Cu–0.12Al$_2$O$_3$ solder approaches to ~79 mm^2, much higher than the original. Hence, solder doped with

0.12 wt% Al$_2$O$_3$ nanoparticles performs the best wettability. In addition, Fig. 5 shows the magnified image of spreading sample of Sn–0.3Ag–0.7Cu–0.5Al$_2$O$_3$ in Fig. 4. Clearly, a relative light-gray wetting ring, a typical capillarity during wetting process emerges, representing one equilibrium state, where the contact angle is usually regarded as zero [35]. However, a white circle surrounded by this wetting ring also emerges, proposed to be Al$_2$O$_3$ agglomerations. After EDX element scanning, it can be judged preliminarily that this white circle surrounded the outer edge of the wetting ring contains elemental Al, O, as shown in Fig. 5c–g. With subsequent EDS analysis of partial area in this region, it can be finally confirmed that Al$_2$O$_3$ agglomerations distributed in this region with some Cu–Sn IMCs formed underneath.

The improvement in wettability contributed by trace amount of nano-Al$_2$O$_3$ particles can be attributed to their inherent surface-active characteristic [19]. As is well-known, surface-active materials (e.g., Al$_2$O$_3$ nanoparticles) are inclined to be adsorbed by grain surfaces of crystal phases due to their high
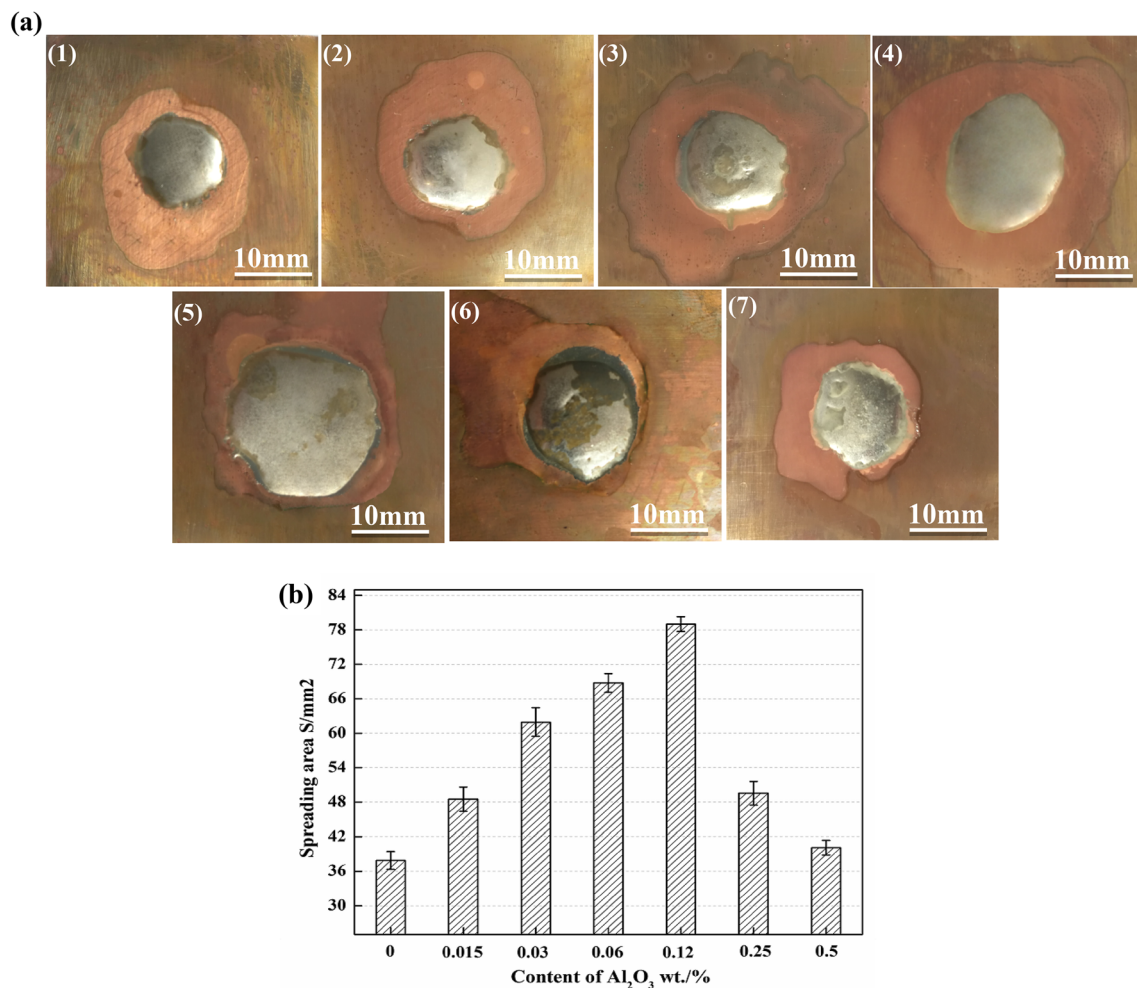
Fig. 4 **a** Representative spreading samples of Sn–0.3Ag–0.7Cu–xnAl$_2$O$_3$ (*1*) x = 0; (*2*) x = 0.015 wt%; (*3*) x = 0.03 wt%; (*4*) x = 0.06 wt%; (*5*) x = 0.12 wt%; (*6*) x = 0.25 wt%; (*7*) x = 0.5 wt%; **b** corresponding bar graph of spreading areas of Sn–0.3Ag–0.7Cu–xAl$_2$O$_3$ (x = 0–0.5 wt%)
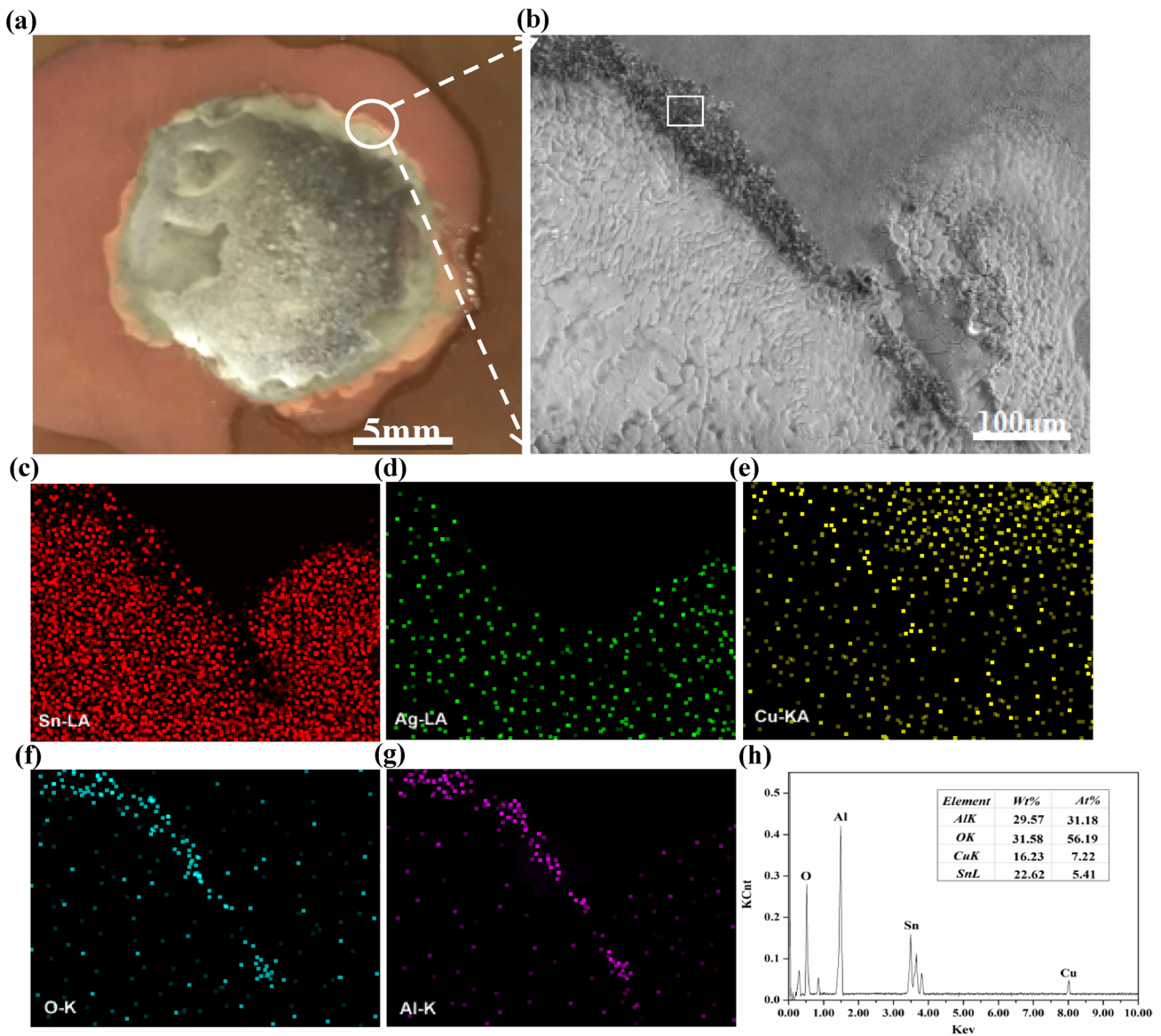
Fig. 5 a Magnified image of spreading sample of Sn–0.3Ag–0.7Cu–0.5Al$_2$O$_3$ in Fig. 4(7); **b** SEM micrograph of selected area marked with white circle in (**a**); **c–g** EDX element mappings of the distri-bution of Sn, Ag, Cu, O, Al, respectively; **h** EDS analysis of area marked with white rectangle in (**b**)

surface free energy [21, 22]. Their adsorption amount at a different grain plane is expressed as below [36]:

$$\Gamma^K = -\frac{C}{RT}\frac{d\gamma^K}{dC}, \tag{2}$$

where Γ^k represents the amount of surface-active materials adsorbed at plane K, C, R, T stand for the content of surface-active materials, the Planck constant and the absolute temperature, respectively, γ^k stands for the surface tension of plane K.

When surface-active materials are adsorbed in plane K, its surface tension will decrease to:
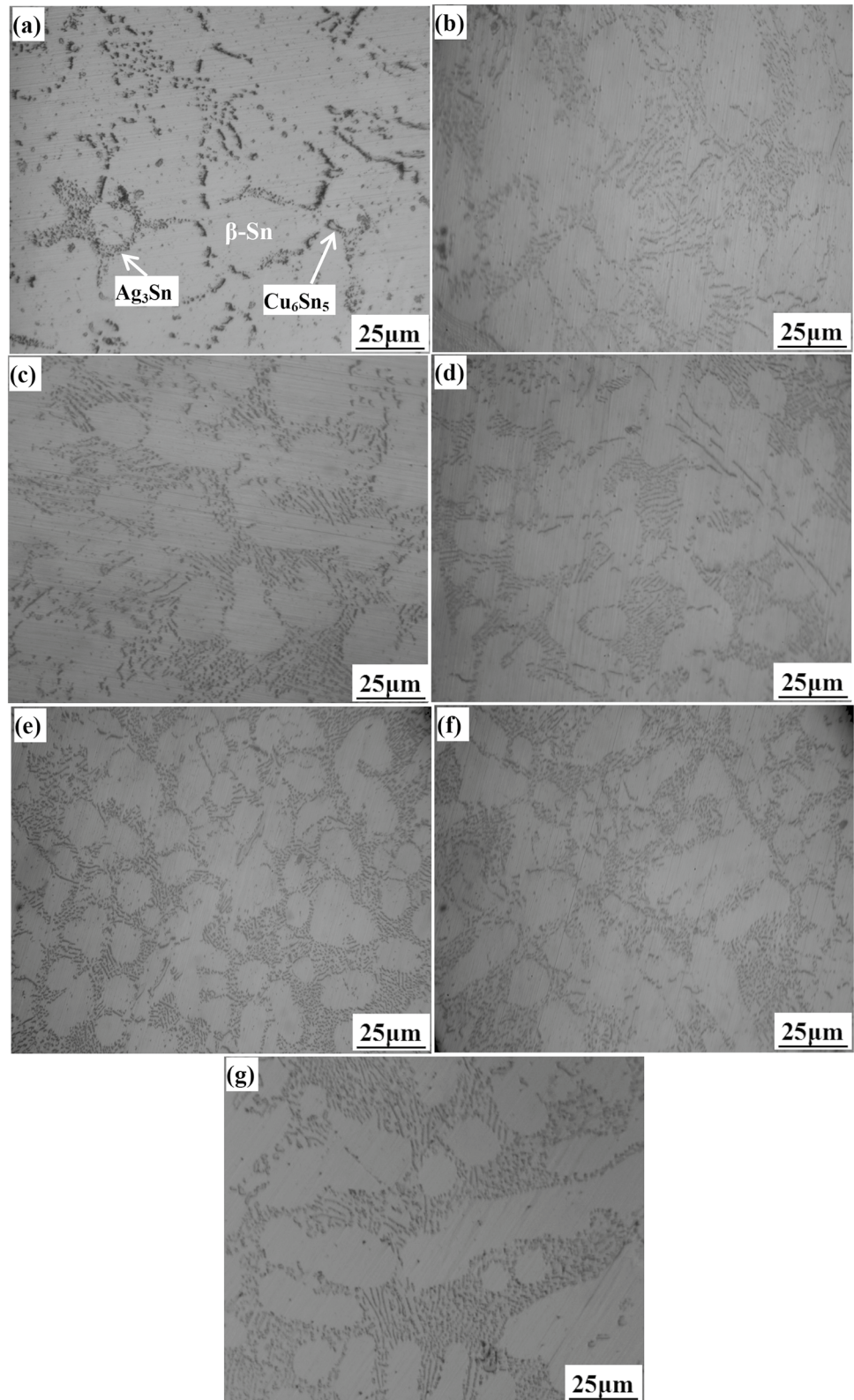
$$\gamma_C^K = \gamma_0^K - RT\int_0^K \frac{\Gamma^K}{C}dC, \tag{3}$$

where γ_0^k is the initial surface tension of plane K without any adsorption. So, the surface free energy of the whole crystalloid (e.g., molten solder) is:

Fig. 6 Schematic diagram of Al_2O_3 nanoparticles **I** at the bottom and **II** at the triple point contributing to wetting and spreading process

$$\sum_K \gamma_C^K A_K = \sum_K \left(\gamma_0^K - RT \int_0^C \frac{\Gamma^K}{C} dC \right) A_K, \tag{4}$$

where A_k is the area of plane K.

Correspondingly, due to the adsorption of α-Al_2O_3 nanoparticles on grain surfaces of Sn–0.3Ag–0.7Cu solder, the surface tension of molten solder (γ_{gl}) will decrease. In order to better understand how α-Al_2O_3 nanoparticles promote the wetting and spreading process of solders, relative schematic diagram is shown in Fig. 6. When molten solder contacts Cu substrate, wetting process begins. In this case, α-Al_2O_3 nanoparticles at the bottom surface of solder (Fig. 6-I) play important roles. They not only decrease the surface tension (γ_{gl}) of solder at this site (explained above) but also have strong tendencies to be adsorbed by Cu substrate, thus can strongly promoting the wetting process. Generally, wetting process is accompanied by spreading process, for the latter of which, α-Al_2O_3 nanoparticles at the triple point (Fig. 6-II) contribute a lot. Al_2O_3 nanoparticles at that site break the system's equilibrium, namely $\gamma_{gl} \cos \theta + \gamma_{ls} = \gamma_{gs}$ [5] (Fig. 2c), where γ_{ls} and γ_{gs} are surface tension of liquid/solid and solid/gas, respectively. So, in order to get a new level of equilibrium, contact angle θ will decrease since nanoparticles can decrease γ_{gl} (explained above) but have no effect on γ_{ls} and γ_{gs}. Consequently, a continued spreading occurs with the achievement of larger spreading area. So, solder performs better wettability with the assistance of α-Al_2O_3 nanoparticles. It should be noted that there exist a most suitable doped content that can maximize the wettability of solder. This is because the surface free energy of the system is prone to reach the minimum, a spontaneous

process. Accordingly, the subtrahend part in Eq. (4) achieves the maximum, shown as follows:

$$\sum_K A_K \int_0^C \frac{\Gamma^K}{C} dC \rightarrow \max. \tag{6}$$

The relation above indicates that planes with the largest Γ^k value had the minimum free energy of the entire interfaces. This is why there exist a most suitable content, found to be 0.12 wt% here. However, once the doping content exceeds the most suitable one (0.12 wt%), the wettability of solder will decline then. This is because the grain surfaces in this case have saturable adsorptions of α-Al_2O_3 nanoparticles and will no longer adsorb any other nanoparticles. So, the remaining α-Al_2O_3 nanoparticles may choose to agglomerate with the adsorbed ones rather than being individually adsorbed by grain surfaces. These agglomerations had a much lower adsorption capacity than α-Al_2O_3 nanoparticles due to their particularly decreased surface free energy caused by the increased sizes. If these agglomerations emerges at the triple point, the spreading process will

Fig. 7 XRD analysis of Sn–0.3Ag–0.7Cu–xAl_2O_3 [x=(*a*) 0; (*b*) 0.015 wt%; (*c*) 0.03 wt%; (*d*) 0.06 wt%; (*e*) 0.12 wt%; (*f*) 0.5 wt%; (*g*) 0.5 wt%]

Fig. 8 Microstructure of Sn–0.3Ag–0.7Cu–xAl$_2$O$_3$ [x=(**a**) 0; (**b**) 0.015 wt%; (**c**) 0.03 wt%; (**d**) 0.06 wt%; (**e**) 0.12 wt%; (**f**) 0.5 wt%; (**g**) 0.5 wt%]

be hindered with the appearance of white circle surrounded the outer edge of the precursor film, as shown in Fig. 5a.
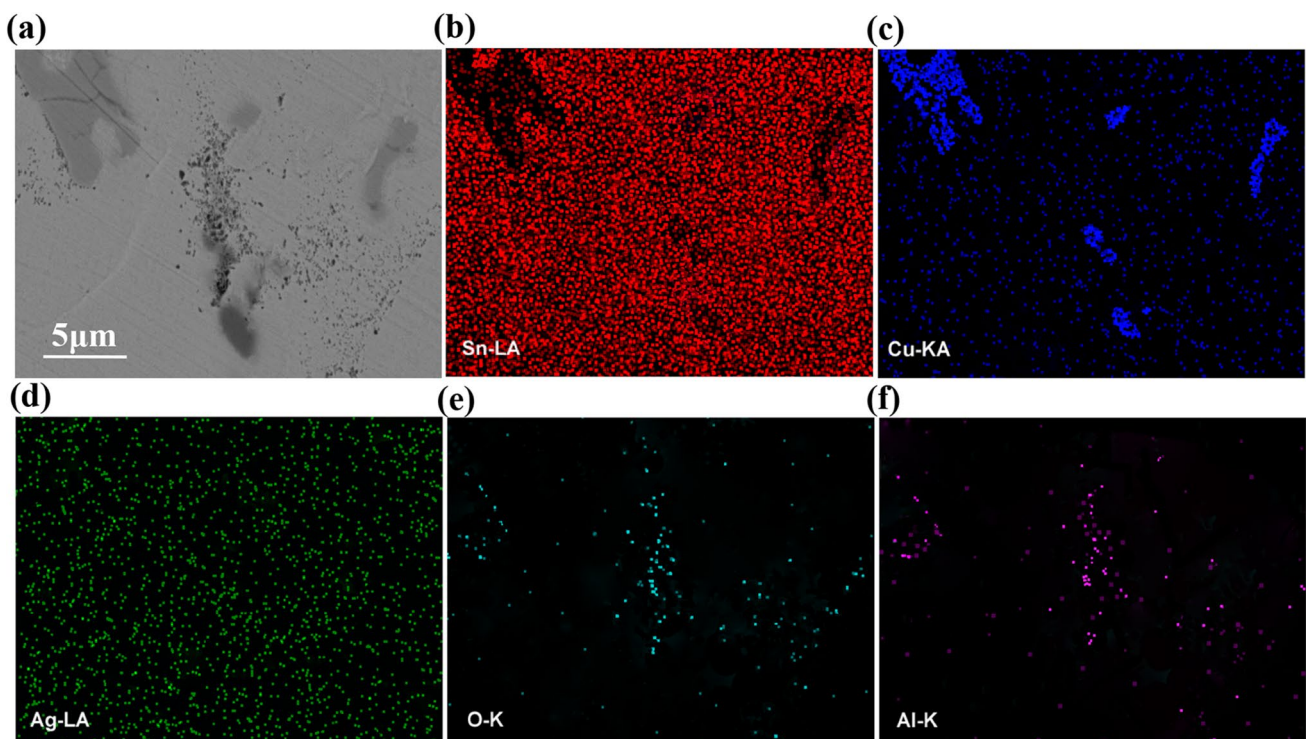
3.3 Microstructure

Figure 7 provides the XRD analyzed results of Sn–0.3Ag–0.7Cu–xAl$_2$O$_3$ solders (x = 0–0.5 wt%) ranging from 20° to 85°. Obviously, diffraction peaks of β-Sn phase and IMCs of Ag$_3$Sn and Cu$_6$Sn$_5$ emerge in all α-Al$_2$O$_3$ nanoparticles-doped Sn–0.3Ag–0.7Cu solders, irrespective of the amount of α-Al$_2$O$_3$. However, some weak peaks corresponding to Al$_2$O$_3$ are detected until the content of Al$_2$O$_3$ nanoparticles reached 0.25 wt% (Fig. 7f, g). This is mainly due to a limitation of XRD technique detecting phases below a certain amount.

In order to further study the influence of various contents of α-Al$_2$O$_3$ nanoparticles on the evolutions of microstructure of solders, observations and analysis with the aid of OM and SEM/EDS were conducted. Figure 8 shows the evolutions of the microstructure of Sn–0.3Ag–0.7Cu–xAl$_2$O$_3$ solders (x = 0–0.5 wt%). It can be observed from Fig. 8a that the microstructure of Sn–0.3Ag–0.7Cu solder consisted of light-gray dendrites (β-Sn) and a dark-gray eutectic region. According to Sn–Ag–Cu ternary phase diagram [37], this eutectic region consists of β-Sn phase and IMCs of dot-like Ag$_3$Sn and Cu$_6$Sn$_5$ with various shapes. These observed

results matched well with the previous XRD analysis results. After doped with trace amount of nano-Al$_2$O$_3$ particles (0.015–0.12 wt%), solders display the evidently refined microstructures with the amount of eutectic areas increasing as well as the size of β-Sn dendrites decreasing (Fig. 8b–e). In addition, IMCs of Ag$_3$Sn and Cu$_6$Sn$_5$ are also remarkably refined. The maximum refinement was realized for solder doped with 0.12 wt% Al$_2$O$_3$ nanoparticles (Fig. 8e). However, a further doping of Al$_2$O$_3$ nanoparticles in turn coarsen the microstructure with β-Sn dendrites becoming large and eutectic region getting sparse (Fig. 8f, g). Figure 9 showed the back scattered electron (BSE) micrograph of the agglomerated phenomenon emerging around Cu$_6$Sn$_5$ IMCs in Sn–0.3Ag–0.7Cu–0.5Al$_2$O$_3$, proposed to be Al$_2$O$_3$ agglomerations, validated by the subsequent EDX element mappings shown in Fig. 9b–f.

Reasons for the refinement in microstructures contributed by doping α-Al$_2$O$_3$ nanoparticles are listed as follows. Firstly, it is because numerous α-Al$_2$O$_3$ nanoparticles in molten alloy serve as extra heterogeneous nucleation sites to accelerate the nucleation process. So, the nucleations of β-Sn phases and IMCs of Ag$_3$Sn and Cu$_6$Sn$_5$ precipitates have inadequate time to grow up. In addition, when surface-active Al$_2$O$_3$ nanoparticles with a suitable amount are doped into solders, they are prone to be adsorbed on the IMCs' surfaces, as shown in Fig. 10. So, the pinning effects on


Fig. 9 **a** Back scattered SEM (BSE) micrograph of Al$_2$O$_3$ agglomerations in the microstructure of Sn–0.3Ag–0.7Cu–0.5Al$_2$O$_3$ solder; EDX element mappings showing the distribution of **b** Sn, **c** Cu, **d** Ag, **e** O and **f** Al element, respectively

grain boundaries' motions will occur, thus hampering IMCs' growth. However, when excessive content of α-Al_2O_3 nanoparticles are doped, partial amount of α-Al_2O_3 nanoparticles will agglomerate with the previous adsorbed ones (Fig. 10c) due to the existence of saturated adsorption quantity on the grain surfaces, as referred in Sect. 3.1. These agglomerations are hard and brittle, which can induce micro-cracks at solder/agglomerations interface and finally deteriorating mechanical properties.

3.4 Shear force and fracture behavior

Figure 11 shows the changes of shear forces with increasing α-Al_2O_3 nanoparticles to 0.5 wt%. Clearly, the shear force of original solder joint is greatly enhanced by minor amount of α-Al_2O_3 nanoparticles-doped, especially as the doped content increases to 0.12 wt%, where the shear force reaches 57.1 N, about 15.3% higher than the non-doped one. However, with increasing α-Al_2O_3 nanoparticles over 0.12 wt%, the shear force of solder joint decreases but still a bit larger than that of the original. In addition, Fig. 12 gives the representative SEM images of fracture surfaces of joint soldered with Sn–0.3Ag–0.7Cu–xAl_2O_3 (x = 0, 0.12, 0.5 wt%). From Fig. 12a, we can clearly see that the fracture surface of the joint soldered with Sn–0.3Ag–0.7Cu presented an extremely elongated slant dimples parallel to shear loading direction with some small regions of river patterns emerging, indicative of a typical mixed fracture mode (ductile and brittle). In addition, region A in Fig. 12a is determined to be pure Sn (Fig. 12f), probably implying that shear cracks occurred mainly at the bulk solder. With 0.12 wt% α-Al_2O_3 nanoparticles doped, the strength of solder increases since
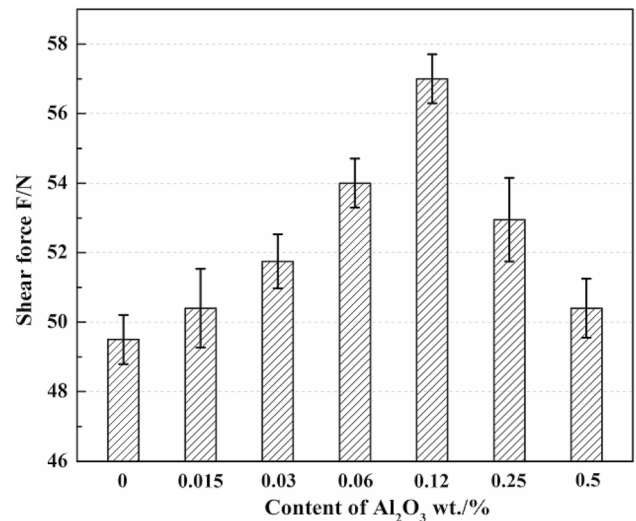
Fig. 11 Shear force evolution of the joints soldered with Sn–0.3Ag–0.7Cu–xAl_2O_3 solders (x = 0–0.5 wt%)

the fracture surface presents much more dimples with evidently decreased size (Fig. 12b). For the fracture behavior of the joint soldered with Sn–0.3Ag–0.7Cu–0.5Al_2O_3, it was judged as ductile fracture mode as well because of the emergence of dimples with various sizes but overall larger than those in the joint fracture soldered with Sn–0.3Ag–0.7Cu–0.12Al_2O_3 (Fig. 12c). In addition, a large amount of hard and brittle agglomerations emerge that may become crack origins, as shown in Fig. 12d, the magnified image of selected area marked in red rectangle in Fig. 12c. After EDS analysis shown in Fig. 12e, these agglomerations
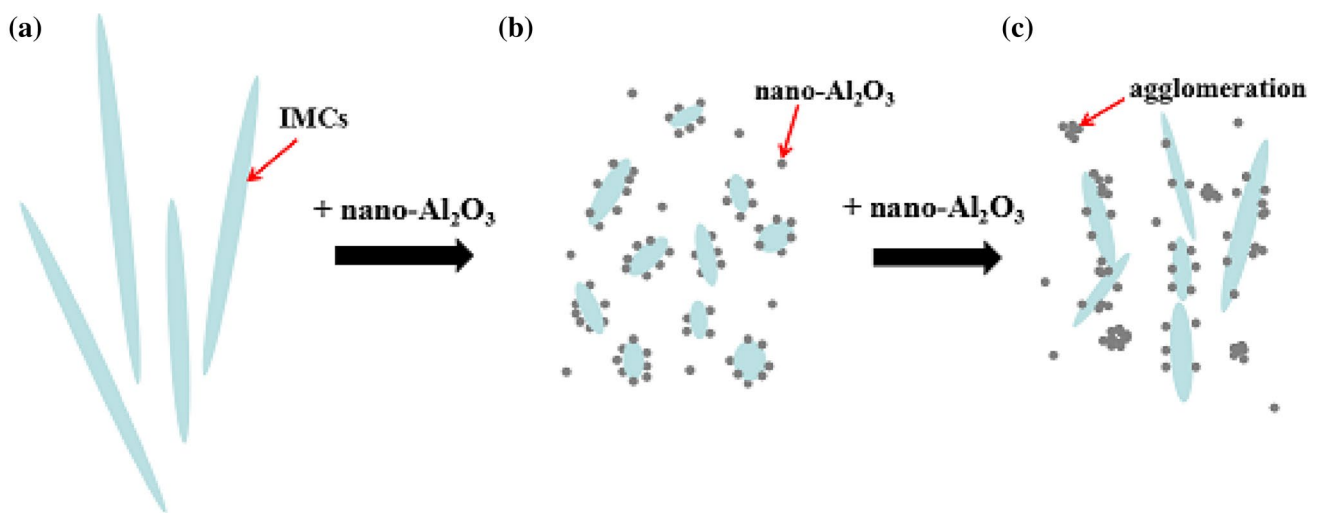
Fig. 10 Schematic diagram of Al_2O_3 nanoparticles refining IMCs in the microstructure of Sn–0.3Ag–0.7Cu–xAl_2O_3 solder: **a** IMCs in the Sn–0.3Ag–0.7Cu solder; **b** IMCs evolution after doping suit-able amount of Al_2O_3 nanoparticles; **c** IMCs evolution after excessive doping of Al_2O_3 nanoparticles
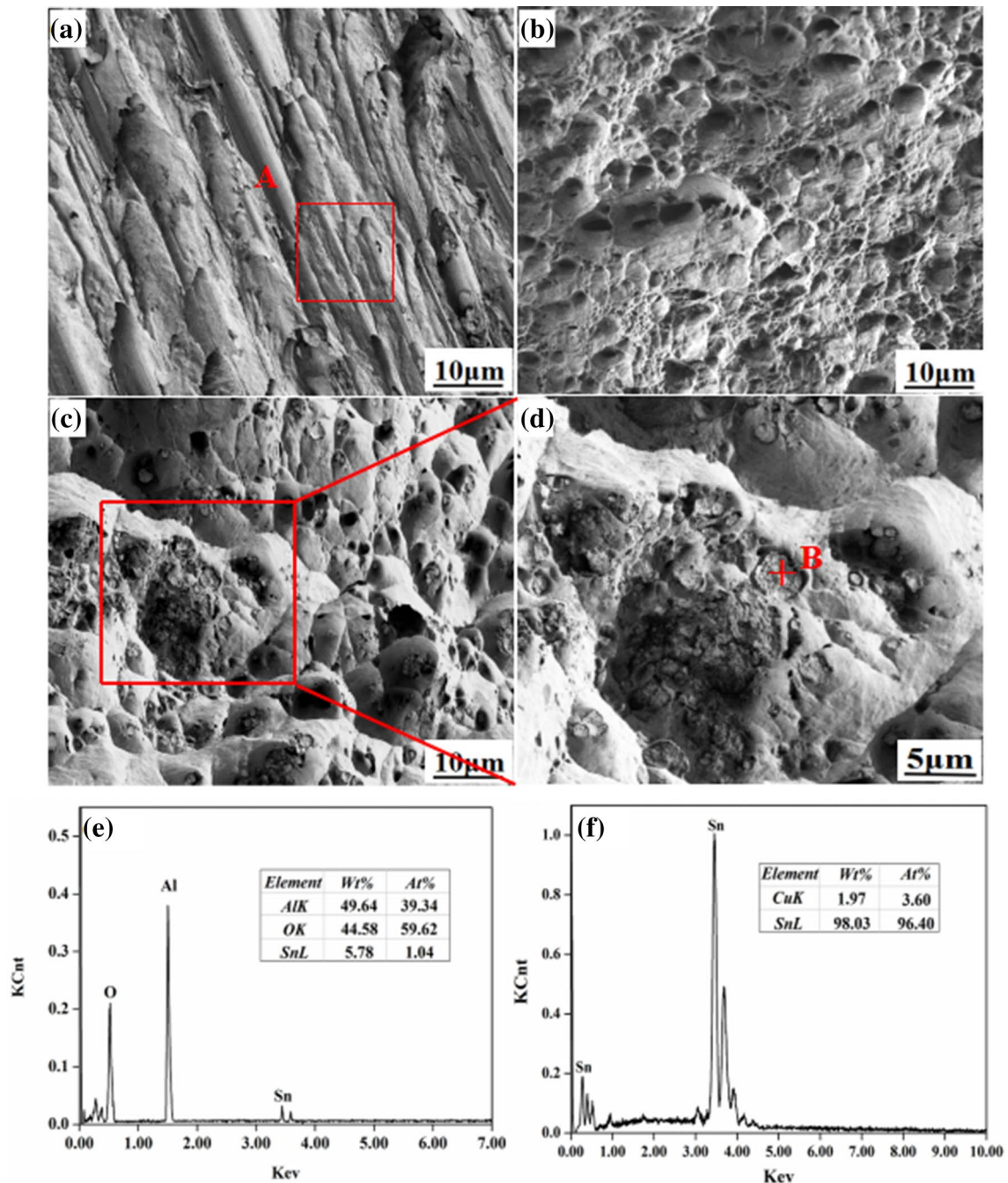
Fig. 12 Fracture morphologies of the joints soldered with Sn–0.3Ag–0.7Cu–xAl$_2$O$_3$ solder: **a** $x = 0$; **b** $x = 0.12$ wt%; **c** $x = 0.5$ wt%; **d** enlarged SEM image of the selected area marked in red rectangle in (**c**), **e** EDS analyzed result of region A in (**a**), **f** EDS analyzed result of point B in (**d**). (Color figure online)

were confirmed as Al$_2$O$_3$, which is the root reason of the evident declining in shear force of solder joints.

Further, the variation in shear forces of solder joints with Al$_2$O$_3$ nanoparticles-doped also closely relates to the evolutions of their interfacial microstructure morphologies. So, the representative interfacial microstructures of the joints soldered with Sn–0.3Ag–0.7Cu–xAl$_2$O$_3$ ($x = 0$,

0.12, 0.5 wt%) are shown in Fig. 13. Clearly, the eutectic structures in the microstructure of the joint soldered with Sn–0.3Ag–0.7Cu solder distribute unevenly with many large acicular Cu$_6$Sn$_5$ IMCs emerging (Fig. 13a). With 0.12 wt% Al$_2$O$_3$ nanoparticles doped, the amount of eutectic structures increases with their distribution becoming more evenly. In addition, Cu$_6$Sn$_5$ IMCs throughout β-Sn matrix are obviously
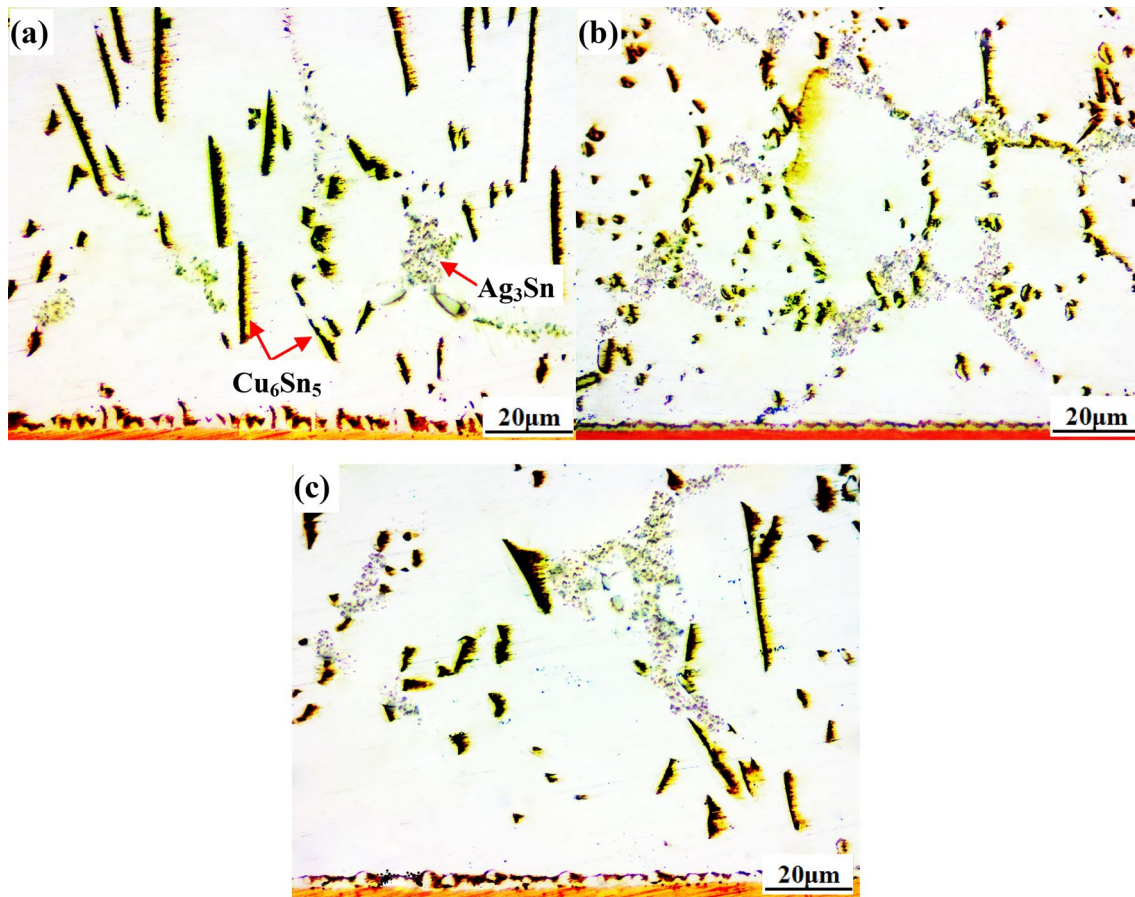
Fig. 13 Interfacial microstructure of the joints soldered with Sn–0.3Ag–0.7Cu–xAl$_2$O$_3$ solder: **a** x = 0; **b** x = 0.12 wt%; **c** x = 0.5 wt%

refined and the amount of nano-Ag$_3$Sn also increases, as shown in Fig. 13b. This is due to the pinning effects on grain boundaries' motions exerted by Al$_2$O$_3$ nanoparticles, as have been detailedly explained in Sect. 3.2. However, with Al$_2$O$_3$ nanoparticles increasing to 0.5 wt%, some large strip-shaped IMCs emerge again (Fig. 13c), relating to the Al$_2$O$_3$ agglomerations with evidently decreased adsorption capacity due to their size increments. In addition, these agglomerations are hard and brittle that can become micro-crack origins and finally degrade the mechanical properties.

Moreover, Fig. 14 shows the BSE micro-graphs of the interfacial IMC layers formed at the interfaces between solder and Cu substrate. Clearly, a continous interfacial IMC layer with average thickness of ~4.94 μm formed at the Sn–0.3Ag–0.7Cu/Cu interface (Fig. 14a). The dark gray protruding portions (marked C) with various irregular shapes nearby the solder side were demonstrated to be Cu$_6$Sn$_5$ IMCs by EDS analysis (Fig. 14d). After optimal amount of Al$_2$O$_3$ nanoparticles-doped (0.12 wt%), the solder/Cu interface displays a much more regular scallop-like interfacial Cu$_6$Sn$_5$ IMCs without any sharp angular (Fig. 14b). Besides, the thickness of interfacial IMC layer decreases to

~2.87 μm, 41.9% thinner than that of non-modified. However, when the doped amount increases to 0.5 wt%, hill-like interfacial IMCs with micro-cracks formed at the solder/Cu interface and the thickness of interfacial IMC layer increases to ~3.66 μm. In addition, black particles aggregate in the grooves between Cu$_6$Sn$_5$ IMCs, proposed to induce the micro-cracks at the solder/Cu interface. After EDS analysis (Fig. 14e), they are confirmed as hard and brittle Al$_2$O$_3$ agglomerations.

The mechanism of how Al$_2$O$_3$ nanoparticles affect interfacial Cu$_6$Sn$_5$ IMCs' growth was explained with aid of the schematic diagram in Fig. 15. With optimal amount of Al$_2$O$_3$ nanoparticles-doped, they will adsorb uniformly on the interfacial Cu$_6$Sn$_5$ IMCs' surfaces (Fig. 15b), causing a pinning effect on the Cu$_6$Sn$_5$ IMCs' growth. Thus, reductions in both fluxes of interfacial reactions and ripening of Cu$_6$Sn$_5$ IMCs occurred, contributing to the decreases in both diameters and thicknesses of interfacial Cu$_6$Sn$_5$ IMCs [38]. The morphology becomes much more regular and thinner than that generates at Sn–0.3Ag–0.7Cu solder/Cu interface. So, the joint soldered with Sn–0.3Ag–0.7Cu–0.12Al$_2$O$_3$ displayed an obviously enhanced shear force. However, when 0.5 wt%
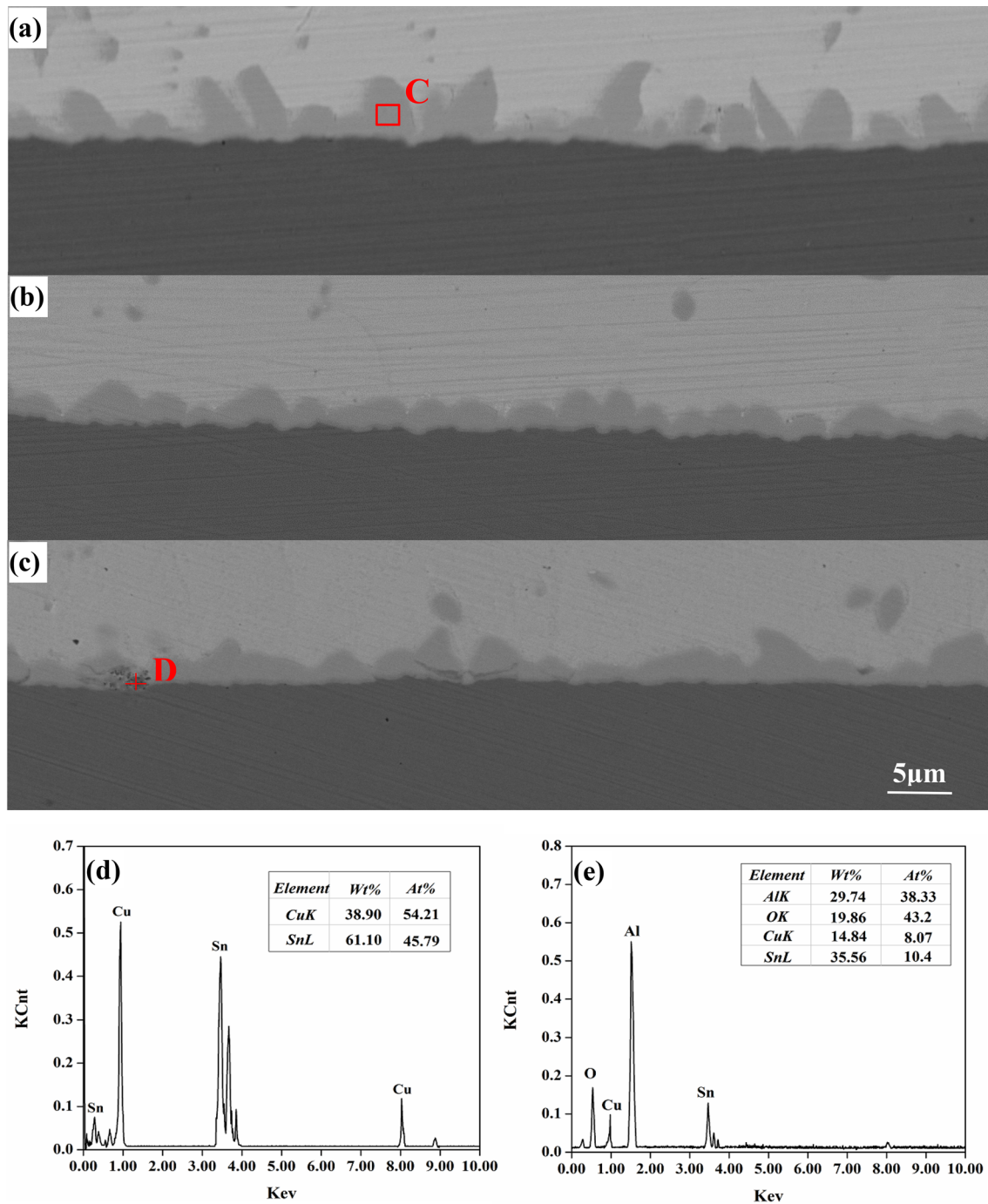
Fig. 14 BSE micrographs of interfacial IMCs at the Sn–0.3Ag–0.7Cu–xAl$_2$O$_3$/Cu interfaces: **a** x=0; **b** x=0.06 wt%; **c** x=0.5 wt%; **d** EDS analyzed result of area C in (**a**), **e** EDS analyzed result of area D in (**c**)

of Al$_2$O$_3$ nanoparticles were doped, agglomerations of them occurred at the Cu$_6$Sn$_5$/solder interface due to their high surface-active characteristic (Fig. 15c), which may become micro-crack origins due to their hard and brittle characteristic. Besides, some interfaces of interfacial Cu$_6$Sn$_5$ IMCs, absent from Al$_2$O$_3$ nanoparticles' adsorption will grow further without any blocks, thus causing the morphology of interfacial IMC layer transforming into hill-like and angular.

In order to quantify the effects of Al$_2$O$_3$ nanoparticles-doped on the growth of interfacial IMC layer, their growth constants are calculated following the classical parabolic equation below [7]:
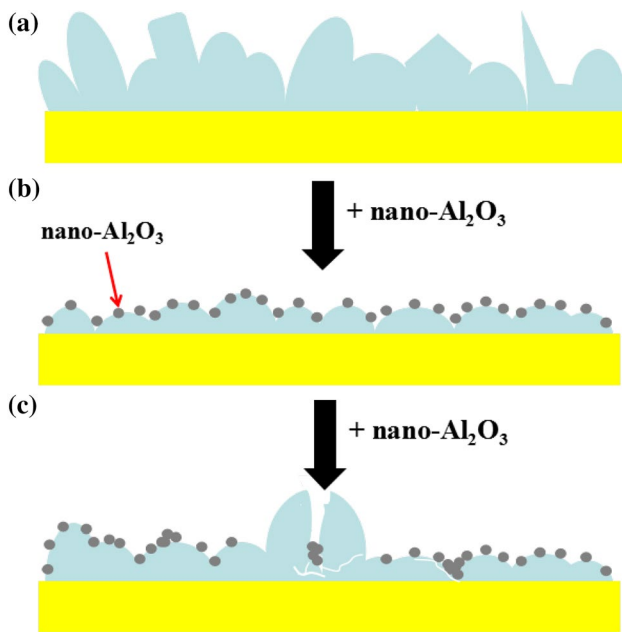
Fig. 15 Schematic diagram of Al$_2$O$_3$ nanoparticles inhibiting interfacial IMC layer growth at Sn–0.3Ag–0.7Cu–xAl$_2$O$_3$/Cu interface: **a** x = 0; **b** x = 0.12 wt%; **c** x = 0.5 wt%

$$x_i = x_0 + \sqrt{Dt}, \tag{7}$$

where x_i is the thickness of interfacial IMC layer after a certain reaction time, x_0 is its initial thickness and here $x_0 = 0$, D relates to the diffusion coefficient of Cu atom into solder and here it means growth rate constant of interfacial IMCs. In addition, t in Eq. (7) is the reaction time. So, by putting the measured thickness and reaction time (~ 480 s) into Eq. (7), the growth rate constant of Cu$_6$Sn$_5$ in different interfaces was calculated to be around 5.08×10^{-10}, 1.71×10^{-10}, 2.79×10^{-10} cm^2/s. Clearly, we can see that suitable amount of Al$_2$O$_3$ nanoparticles-doped largely decrease the growth rate constant of interfacial Cu$_6$Sn$_5$ IMCs.

4 Conclusions

In this study, the evolutions and changes of the microstructures and properties of Sn–0.3Ag–0.7Cu–xAl$_2$O$_3$ low-Ag solders (x = 0–0.5 wt%) applied in electronic applications were investigated. Based on the above experimental results and analysis, conclusions drawn were listed below:

(1) The melting point of Sn–0.3Ag–0.7Cu solder has negligible change after trace amount of Al$_2$O$_3$ nanoparticles doped, while its undercooling can be obviously lowered down and with the minimum value (5.9 °C) achieved by the solder doped with 0.12 wt% Al$_2$O$_3$ nanoparti-

cles. In addition, Sn–0.3Ag–0.7Cu–0.12Al$_2$O$_3$ solder also performed the best wettability with spreading area reaching the maximum value (~ 79 mm^2).

(2) Correspondingly, the joint soldered with Sn–0.3Ag–0.7Cu–0.12Al$_2$O$_3$ displays the maximum shear force (57.1 N) due to the gaining of the most refined microstructure as well as the most regular interfacial morphology with the smallest thickness (~ 2.87 μm). In addition, theoretical analysis also shows 0.12 wt% Al$_2$O$_3$ nanoparticles can decreases the growth rate constant of interfacial Cu$_6$Sn$_5$ IMCs from 5.08×10^{-10} to 1.71×10^{-10} cm^2/s, once again demonstrating the effective inhibition effect on interfacial Cu$_6$Sn$_5$ IMCs' growth contributed by 0.12 wt% Al$_2$O$_3$ nanoparticles-doped.

(3) Further, after 0.12 wt% Al$_2$O$_3$ nanoparticles was doped, the fracture mode of solder changed from mixed fracture failure of ductile and brittle to ductile fracture failure. However, excessive Al$_2$O$_3$ nanoparticles-doped in turn decline the ductility of solder due to the emergence of hard and brittle Al$_2$O$_3$ agglomerations.

References

1. V. Eveloy, S. Ganesan, Y. Fukuda, J. Wu, M.G. Pecht, *2005 6th International Conference on Electronic Packaging Technology* (2005), pp. 27–44. https://doi.org/10.1109/ICEPT.2005.1564718
2. S. Cheng, C.M. Huang, M. Pecht, Microelectron. Reliab. **75**, 77–95 (2017)
3. J. Wang, H.M. Wei, P. He, T.S. Lin, F.J. Lu, J. Electron. Mater. **44**(10), 3872–3879 (2015)
4. M.L. Huang, N. Zhao, S. Liu, Y.Q. He, Trans. Nonferrous Met. Soc. China **26**(6), 1663–1669 (2016)
5. H.W. Chiang, K. Chang, J.Y. Chen, J. Electron. Mater. **35**(12), 2074–2080 (2016)
6. F.X. Che, W.H. Zhu, S.W. Edith, X.W. Poh, X.R. Zhang, Zhang, J. Alloy. Compd. **507**(1), 215–224 (2010)
7. M. Yang, Y.H. Ko, J.H. Bang, T.S. Kim, C.W. Lee, M.Y. Li, Mater. Charact. **124**, 250–259 (2017)
8. G. Zeng, S.B. Xue, L. Zhang, L.L. Gao, W. Dai, J.D. Luo, J. Mater. Sci. Mater. Electron. **21**(5), 421–440 (2010)
9. A.A. El-Daly, A.M. El-Taher, S. Gouda, Mater. Des. **65**, 796–805 (2015)
10. A.E. Hammad, Mater. Des. **52**, 663–670 (2013)
11. A.A. El-Daly, A.E. Hammad, G.S. Al-Ganainy, M. Ragab, Mater. Sci. Eng. A **608**, 130–138 (2014)
12. J. Wu, S.B. Xue, J.W. Wang, J.X. Wang, S. Liu, J. Mater. Sci. Mater. Electron. **28**(14), 10230–10244 (2017)
13. J.C. Xu, S.B. Xue, P. Xue, W.M. Long, Q.K. Zhang, J. Mater. Sci. Mater. Electron. **27**(8), 8771–8777 (2016)
14. W.X. Chen, S.B. Xue, H. Wang, Y.H. Hu, J.X. Wang, J. Mater. Sci. Mater. Electron. **21**(7), 719–725 (2010)

15. Q.K. Zhang, W.M. Long, X.Q. Yu, Y.Y. Pei, P.X. Qiao, J. Alloy. Compd. **622**, 973–978 (2015)
16. Y.L. Huang, Z.Y. Xiu, G.H. Wu, Y.H. Tian, P. He, J. Mater. Sci. Mater. Electron. **27**(7), 6809–6815 (2016)
17. X.L. Qiu, H.M. Wei, Q. Wang, P. He, T.S. Lin, F.J. Lu, Mater. Sci. Technol. **23**(1), 20–24 (2015)
18. X.C. Lv, T.S. Lin, J. Wang, A. Jing, P. He, Mater. Trans. **54**(7), 1228–1231 (2013)
19. L. Zhang, K.N. Tu, Mater. Sci. Eng. R **82**(1), 1–32 (2014)
20. T. Fouzder, Q.Q. Li, Y.C. Chan, D.K. Chan, J. Mater. Sci. Mater. Electron. **25**(9), 4012–4023 (2014)
21. L. Zhang, X.Y. Fan, Y.H. Guo, C.W. He, Electron. Mater. Lett. **10**(3), 645–647 (2014)
22. X.D. Liu, Y.D. Han, H.Y. Jing, J. Wei, L.Y. Xu, Mater. Sci. Eng. A **562**, 25–32 (2013)
23. K.M. Kumar, V. Kripesh, A.A.O. Tay, J. Alloy. Compd. **450**(1–2), 229–237 (2008)
24. Z.B. Yang, W. Zhou, P. Wu, Mater. Sci. Eng. A **590**, 295–300 (2014)
25. A.K. Gain, Y.C. Chan, W.K.C. Yung, Microelectron. Reliab. **51**(12), 2306–2313 (2011)
26. A. Fawzy, S.A. Fayek, M. Sobhy, E. Nassr, M.M. Mousa, G. Saad, J. Mater. Sci. Mater. Electron. **24**(9), 3210–3218 (2013)
27. L. Sun, L. Zhang, L. Xu, S.J. Zhong, J. Ma, B. Li, J. Mater. Sci. Mater. Electron. **27**(7), 7665–7673 (2016)
28. L. Yang, J.G. Ge, Y.C. Zhang, J. Dai, Y.F. Jing, J. Mater. Sci. Mater. Electron. **26**(1), 613–619 (2015)
29. Y. Gu, X.C. Zhao, Y. Li, Y. Liu, Y. Wang, Z.Y. Li, J. Alloy. Compd. **627**, 39–47 (2015)
30. W.Q. Xing, X.Y. Yu, H. Li, L. Ma, W. Zuo, P. Dong, W.X. Wang, M. Ding, J. Alloy. Compd. **695**, 574–582 (2017)
31. L.C. Tsao, R.W. Wu, T.H. Cheng, K.H. Fan, R.S. Chen, Mater. Des. **50**(17), 774–781 (2013)
32. J. Xiao, Y. Wan, J. Li, Chin. J. Nonferrous Met. **16**(12), 2120–2125 (2016)
33. C.J. Lu, Z.Z. Zhang, J.Q. Zhou, S.M. Zhang, Mater. Rev. **21**(8), 165–166 (2007)
34. R.N. Han, S.B. Xue, Y.H. Hu, Z.Y. Wang, J.Y. Ja, Trans. China Weld. Inst. **33**(10), 101–104 (2012)
35. W.E. Rd, G.S. Grest, D.R. Heine, Phys. Rev. Lett. **91**(23), 236102 (2003)
36. Q.J. Zhai, S.K. Guan, Q.Y. Shang, *Calphad-Computer Coupling of Phase Diagrams & Thermochemistry* (Industry Press, Beijing, 1999), p. 142
37. A. Roshanghias, J. Vrestal, A. Yakymovych, K.W. Richter, H. Ipser, Calphad **49**, 101–109 (2015)
38. H.K. Kim, T.N. Tu, Phys. Rev. B **53**(23), 16027–16034 (1996)